PHOTONICS Research

Inverse-designed photonic fibers and metasurfaces for nonlinear frequency conversion [Invited]

Chawin Sitawarin,[1] Weiliang Jin,[1] Zin Lin,[2] and Alejandro W. Rodriguez[1,*]

[1]Department of Electrical Engineering, Princeton University, Princeton, New Jersey 08544, USA
[2]John A. Paulson School of Engineering and Applied Sciences, Harvard University, Cambridge, Massachusetts 02138, USA
*Corresponding author: arod@princeton.edu

Received 22 November 2017; revised 19 March 2018; accepted 20 March 2018; posted 21 March 2018 (Doc. ID 313902); published 20 April 2018

Typically, photonic waveguides designed for nonlinear frequency conversion rely on intuitive and established principles, including index guiding and bandgap engineering, and are based on simple shapes with high degrees of symmetry. We show that recently developed inverse-design techniques can be applied to discover new kinds of microstructured fibers and metasurfaces designed to achieve large nonlinear frequency-conversion efficiencies. As a proof of principle, we demonstrate complex, wavelength-scale chalcogenide glass fibers and gallium phosphide three-dimensional metasurfaces exhibiting some of the largest nonlinear conversion efficiencies predicted thus far, e.g., lowering the power requirement for third-harmonic generation by 10^4 and enhancing second-harmonic generation conversion efficiency by 10^7. Such enhancements arise because, in addition to enabling a great degree of tunability in the choice of design wavelengths, these optimization tools ensure both frequency- and phase-matching in addition to large nonlinear overlap factors.

OCIS codes: (050.1755) Computational electromagnetic methods; (060.4370) Nonlinear optics, fibers; (190.2620) Harmonic generation and mixing; (190.4360) Nonlinear optics, devices; (350.4238) Nanophotonics and photonic crystals.

https://doi.org/10.1364/PRJ.6.000B82

1. INTRODUCTION

Nonlinear frequency conversion plays a crucial role in many photonic applications, including ultra-short pulse shaping [1,2], spectroscopy [3], generation of novel optical states [4–6], and quantum information processing [7–9]. Although frequency conversion has been studied exhaustively in bulky optical systems, including large ring resonators [10] and etalon cavities [11], it remains largely unstudied in micro- and nano-scale structures where light can be confined to lengthscales of the order of or even smaller than its wavelength. By confining light over long a time and to small volumes, such highly compact devices greatly enhance light–matter interactions, enabling similar as well as new [12] functionalities compared to those available in bulky systems but at much lower power levels. Several proposals have been put forward based on the premise of observing enhanced nonlinear effects in structures capable of supporting multiple resonances at far-away frequencies [13–21], among which are micro-ring resonators [22,23] and photonic crystal (PhC) cavities [24,25]. However, to date, these conventional designs fall short of simultaneously meeting the many design challenges associated with resonant frequency conversion, chief among them being the need to support multiple modes with highly concentrated fields, exactly matched resonant frequencies, and strong mode overlaps [26]. Recently, we proposed to leverage powerful, large-scale optimization techniques (commonly known as inverse design) to allow computer-aided photonic designs that can address all of these challenges.

Our recently demonstrated optimization framework allows automatic discovery of novel cavities that support tightly localized modes at several desired wavelengths and exhibit large nonlinear mode overlaps. As a proof-of-concept, we proposed doubly resonant structures, including multi-layered, aperiodic micro-post cavities and multi-track ring resonators, capable of realizing second-harmonic generation efficiencies exceeding 10^4 W^{-1} [27,28]. In this paper, we extend and apply this optimization approach to design extended structures, including micro-structured optical fibers and PhC three-dimensional metasurfaces, as shown in Fig. 1, for achieving high-efficiency (second- and third-harmonic) frequency conversion. Harmonic generation, which underlies numerous applications in science, including coherent light sources [29], optical imaging and microscopy [30,31], and entangled-photon generation [32], is now feasible at lower power requirements thanks to the availability of highly nonlinear $\chi^{(2)}$ and $\chi^{(3)}$ materials such as III–V semiconductor compounds [33,34] and novel types of chalcogenide glasses [35]. In combination with advances in materials synthesis, emerging fabrication technologies have also

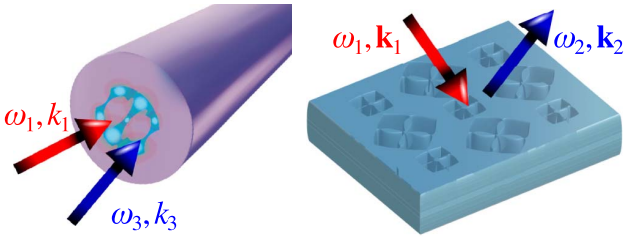

Fig. 1. Schematic illustration of third-harmonic generation and second-harmonic generation processes in inverse-designed microstructured fibers and metasurfaces, respectively.

enabled demonstrations of sophisticated micro-structured fibers [36] and metasurfaces [37–44], paving the way for experimental realization of inverse-designed structures of increased geometric and fabrication complexity, which offer orders-of-magnitude enhancements in conversion efficiencies and the potential for augmented functionalities.

Given a material system of intrinsic $\chi^{(2)}$ or $\chi^{(3)}$ nonlinear coefficient, the efficiency of any given frequency-conversion process in a resonant geometry will be determined by a few modal parameters. The possibility of confining light within small mode volumes over a long time or distance leads to significant gains in efficiency (i.e., lower power requirements), stemming from the higher intensity and cascadability of nonlinear interactions (compensating for the otherwise small bulk nonlinearities). In particular, the efficiency of such resonant processes depends on the product of mode lifetimes and a nonlinear coefficient β, given by Eqs. (6) and (8) below, which generalizes the familiar concept of quasi-phase-matching to situations that include wavelength-scale resonators [26]. For propagating modes, leaky or guided, the existence of a propagation phase further complicates this figure of merit, with optimal designs requiring: (i) phase-matching and frequency-matching conditions, (ii) large nonlinear mode overlaps β, and (iii) large dimensionless lifetimes Q (low material absorption and/or radiative losses in the case of leaky modes). The main design challenge is the difficult task of forming a doubly resonant cavity with far-apart modes that simultaneously exhibit long lifetimes and large β, along with phase and frequency matching. To date, the majority of prior works on frequency conversion in fibers [45–47] and metasurfaces [38–40,42,48–51] have focused on only one of these aspects (usually phase matching) while ignoring the others. The geometries discovered by our optimization framework, in contrast, address the above criteria, revealing complex fibers and metasurfaces supporting TE or TM modes with guaranteed phase and frequency matching, long lifetimes Q, and enhanced overlap factors β at any desired propagation wavevector, and resulting in orders-of-magnitude enhancements in conversion efficiencies.

2. OVERVIEW OF OPTIMIZATION

The possibility of fine-tuning spatial features of photonic devices to realize functionalities not currently achievable by conventional optical design methodologies based on index guiding and bandgap confinement (which work exceedingly well but are otherwise limited for narrowband applications) has been a major drive behind the past several decades of interest in the topic of photonic optimization [52,53]. Among these techniques are probabilistic Monte Carlo algorithms, e.g., particle swarms, simulated annealing, and genetic algorithms [54–56]. Though sufficient for the majority of narrowband (single-mode) applications, many of these gradient-free methods are limited to typically small sets of design parameters [57] that often prove inadequate for handling wideband (multi-mode) problems. On the other hand, gradient-based inverse-design techniques are capable of efficiently exploring a much larger design space by making use of analytical derivative information of the specified objective and constraint functions [58], demonstrated to be feasible for as many as 10^9 design variables [59]. Recently, the development of versatile mathematical programming methods and the rapid growth in computational power have enabled concurrent progress in photonic inverse design, allowing theoretical (and more recently, experimental) demonstrations of complex topologies and unintuitive geometries with unprecedented functionalities that would be arguably difficult to realize through conventional intuition alone. However, to date, most applications of inverse design in photonics are confined to linear devices such as mode converters, waveguide bends, and beam splitters [57,58,60–65]. We believe that this paper along with our recent works [27,28] provides a glimpse of the potential of photonic optimization in nonlinear optics.

A typical optimization problem seeks to maximize or minimize an objective function f, subject to certain constraints g, over a set of free variables or degrees of freedom (DOFs) [66]. Generally, one can classify photonic inverse design into two different classes of optimization strategies, based primarily on the nature or choice of DOF [67]. Given a computational domain or grid, the choice of a finite-dimensional parameter space not only determines the degree of complexity but also the convergence and feasibility of the solutions. One possibility is to exploit each DOF in the computational domain as an optimization parameter, known as topology optimization (TO), in which case one typically (though not always) chooses the dielectric permittivity of each pixel $\epsilon(\mathbf{r})$ as a DOF (known as a continuous relaxation parameter [68]). Another possibility, known as shape optimization, is to expand the optimization parameter space in a finite set of shapes (independent of the computational discretization), which may be freeform contours represented by so-called level sets [69] (the level-set method) or basic geometric entities with simpler parametrizations (e.g., polytopes) [70]. In the level-set method, the zeros of a level-set "function" $\Phi(\mathbf{r})$ define the boundaries of "binary shapes"; the optimization then proceeds via a level-set partial differential equation characterized by a velocity field, which is, in turn, constructed from derivative information [69]. A much simpler variant (which we follow) is to choose a fixed but sufficient number of basic binary shapes whose parameters can be made to evolve by an optimization algorithm. Essentially, for such a parametrization, the mathematical representations of the shapes must yield continuous (analytic) derivatives, which is not feasible a priori due to the finite computational discretization and

can instead be enforced by the use of a "smoothing kernel" (described below).

A generic TO formulation is written down as

$$\max / \min\ f(\overline{\epsilon}_\alpha), \tag{1}$$

$$g(\overline{\epsilon}_\alpha) \le 0, \tag{2}$$

$$0 \le \overline{\epsilon}_\alpha \le 1, \tag{3}$$

where the DOFs are the normalized dielectric permittivities $\overline{\epsilon}_\alpha \in [0,1]$ assigned to each pixel or voxel (indexed α) in a specified volume [58,60]. The subscript α denotes appropriate spatial discretization $\mathbf{r} \to (i,j,k)_\alpha \Delta$ with respect to Cartesian or curvilinear coordinates. Depending on the choice of background (bg) and structural materials, $\overline{\epsilon}_\alpha$ is mapped onto a position-dependent dielectric constant via $\epsilon_\alpha = (\epsilon - \epsilon_{\mathrm{bg}}\overline{\epsilon}_\alpha + \epsilon_{\mathrm{bg}})$. The binarity of the optimized structure is enforced by penalizing the intermediate values $\overline{\epsilon} \in (0,1)$ or utilizing a variety of filter and regularization methods [58]. Starting from a random initial guess, the technique discovers complex structures automatically with the aid of powerful gradient-based algorithms such as the method of moving asymptotes (MMA) [71]. For an electromagnetic problem, f and g are typically functions of the electric $\mathbf{E}$ or magnetic $\mathbf{H}$ fields integrated over some region, which are in turn solutions of Maxwell's equations under some incident current or field. In what follows, we exploit direct solution of frequency-domain Maxwell's equations

$$\nabla \times \frac{1}{\mu}\nabla \times \mathbf{E} - \epsilon(\mathbf{r})\omega^2 \mathbf{E} = i\omega \mathbf{J}, \tag{4}$$

describing the steady-state field $\mathbf{E}(\mathbf{r};\omega)$ in response to incident currents $\mathbf{J}(\mathbf{r},\omega)$ at frequency ω. While solution of Eq. (4) is straightforward and commonplace, the key to making optimization problems tractable is to obtain a fast-converging and computationally efficient adjoint formulation of the problem. Within the scope of TO, this requires efficient calculations of the derivatives $\frac{\partial f}{\partial \overline{\epsilon}_\alpha}$, $\frac{\partial g}{\partial \overline{\epsilon}_\alpha}$ at every pixel α, which we perform by exploiting the adjoint-variable method (AVM) [58].

While the TO technique is quite efficient in handling the enormity of an unconstrained design space, it often leads to geometries with irregular features that are difficult to fabricate. An alternative approach that is in principle more conducive to fabrication constraints is to exploit shape optimization. In this work, we primarily focus on a simple implementation of the latter that employs a small and, hence, limited set of elementary geometric shapes, e.g., ellipses [72] and polytopes, parametrized by a few DOFs. In particular, we express the dielectric profile of the computational domain as a sum of basic shape functions with permittivities, $\overline{\epsilon}_\alpha = \sum_\beta H_\beta(\mathbf{r}_\alpha;\{p_\beta\})$, described by shape functions H_β and a finite set of geometric parameters $\{p_\beta\}$, where β denotes the shape index. Here, to deal with potential overlap of two or more shapes, we implement a filter function that enforces the same maximum-permittivity constraint $\overline{\epsilon} \le 1$ described above. The derivatives of a given objective function f (and associated constraints) can then be obtained via the chain rule $\frac{\partial f}{\partial p_i} = \frac{\partial f}{\partial \overline{\epsilon}_\alpha}\frac{\partial \overline{\epsilon}_\alpha}{\partial p_i}$, where the smoothness of the derivatives is guaranteed by insisting that the shape functions H be continuously differentiable functions. Below, we choose non-piecewise-constant ellipsoidal shapes with exponentially varying dielectric profiles near the boundaries, the smoothness of which is determined by a few simple parameters that can, at various points along the optimization, be slowly adjusted to realize fully binary structures upon convergence. Such a "relaxation" process [70] is analogous to the application of a binary filter in the objective function [58].

Any nonlinear frequency conversion process can be viewed as a frequency mixing scheme in which two or more constituent photons at a set of frequencies $\{\omega_n\}$ interact to produce an output photon at frequency $\Omega = \sum_n c_n \omega_n$, where $\{c_n\}$ can be either negative or positive, depending on whether the corresponding photons are created or destroyed in the process [73]. Given an appropriate nonlinear tensor component $\chi_{ijk\ldots}$, with $i,j,k,\ldots \in \{x,y,z\}$, mediating an interaction between the field components $E_i(\Omega)$ and $E_{1j}, E_{2k}, \ldots$, we begin with a collection of point dipole currents, each at the constituent frequency $\omega_n, n \in \{1,2,\ldots\}$, such that $\mathbf{J}_n = \hat{\mathbf{e}}_{n\nu}\delta(\mathbf{r}-\mathbf{r}')$, where $\hat{\mathbf{e}}_{n\nu} \in \{\hat{\mathbf{e}}_{1j}, \hat{\mathbf{e}}_{2k}, \ldots\}$ is a polarization vector chosen so as to excite the desired electric-field polarization components (ν) of the corresponding mode at an appropriate position $\mathbf{r}'$. Given the choice of incident currents $\mathbf{J}_n$, we solve Maxwell's equations to obtain the corresponding constituent electric-field response $\mathbf{E}_n$, from which one can construct a nonlinear polarization current $\mathbf{J}(\Omega) = \overline{\epsilon}(\mathbf{r})\prod_n E_{n\nu}^{|c_n|(*)}\hat{\mathbf{e}}_i$, where $E_{n\nu} = \mathbf{E}_n \cdot \hat{\mathbf{e}}_{n\nu}$ and $\mathbf{J}(\Omega)$ can be generally polarized $(\hat{\mathbf{e}}_i)$ in a (chosen) direction that differs from the constituent polarizations $\hat{\mathbf{e}}_{n\nu}$. Here, $(*)$ denotes complex conjugation for negative c_n and no conjugation otherwise. Finally, maximizing the radiated power, $-\mathrm{Re}[\int \mathbf{J}(\Omega)^* \cdot \mathbf{E}(\Omega)\mathrm{d}\mathbf{r}]$, due to $\mathbf{J}(\Omega)$, one is immediately led to the following nonlinear optimization problem:

$$\begin{aligned}
&\max_{\overline{\epsilon}} f(\overline{\epsilon};\omega_n) = -\mathrm{Re}\left[\int \mathbf{J}(\Omega)^* \cdot \mathbf{E}(\Omega)\mathrm{d}\mathbf{r}\right],\\
&\mathcal{M}(\overline{\epsilon},\omega_n)\mathbf{E}_n = i\omega_n \mathbf{J}_n, \qquad \mathbf{J}_n = \hat{\mathbf{e}}_{n\nu}\delta(\mathbf{r}-\mathbf{r}'),\\
&\mathcal{M}(\overline{\epsilon},\Omega)\mathbf{E}(\Omega) = i\Omega\mathbf{J}(\Omega), \qquad \mathbf{J}(\Omega) = \overline{\epsilon}\prod_n E_{n\nu}^{|c_n|(*)}\hat{\mathbf{e}}_i,\\
&\mathcal{M}(\overline{\epsilon},\omega) = \nabla \times \frac{1}{\mu}\nabla \times -\epsilon(\mathbf{r})\omega^2,
\end{aligned} \tag{5}$$

where $\overline{\epsilon}$ is given by either the topology or shape parameterizations described above. Writing down the objective function in terms of the nonlinear polarization currents, it follows that solution of Eq. (5), obtained by employing any mathematical programming technique that makes use of gradient information, e.g., the AVM [58], maximizes the nonlinear coefficient (mode overlap) associated with the aforementioned nonlinear optical process. The above framework can be easily extended to consider propagating modes once we take into account the appropriate Bloch boundary conditions that may arise from any desired wave vectors imposed at the requisite frequencies [74]. In the case of optical fibers or PhC metasurfaces (or, more generally, any waveguiding system), such an extension naturally guarantees perfect phase and frequency matching of the relevant modes in the optimized structure.

3. THIRD-HARMONIC GENERATION IN FIBERS

Conventional microstructured fibers (e.g., Bragg and holey fibers) are typically designed based on intuitive principles like

slow light [47], index guiding, and bandgap confinement [52], and thus often consist of periodic cross sections comprising simple shapes [75,76]. Below, we apply the aforementioned optimization techniques to propose much more complicated heterostructure fibers designed to enhance third-harmonic generation at any desired wavelength. To achieve large third-harmonic generation efficiencies, the fiber must support two co-propagating modes of frequencies ω_1 and $\omega_3 = 3\omega_1$ and wavenumbers that satisfy the phase-matching condition $k_3 = 3k_1$. Furthermore, the system must exhibit low radiative/dissipative losses or, alternatively, attenuation lengths that are much longer than the corresponding interaction lengths L, defined as the propagation length at which 50% of the fundamental mode is upconverted. In the small-input signal regime, the converted third-harmonic output power $P_3 \propto P_1^2$ and the interaction length $L = \frac{16}{3k_1 Z_0 |\beta_3| P_1}$ depend on the incident power P_1, vacuum impedance Z_0, and nonlinear overlap factor [77]

$$\beta_3 = \frac{\oiint \chi^{(3)} (\mathbf{E}_1^* \cdot \mathbf{E}_3)(\mathbf{E}_1^* \cdot \mathbf{E}_1^*) \mathrm{d}S}{\left(\mathrm{Re}\left[\frac{1}{2} \oiint \sqrt{(\mathbf{E}_1^* \times \mathbf{H}_1) \cdot \hat{z}} \mathrm{d}S \right] \right)^3 \sqrt{\mathrm{Re}\left[\frac{1}{2} \oiint (\mathbf{E}_3^* \times \mathbf{H}_3) \cdot \hat{z} \mathrm{d}S \right]}}, \tag{6}$$

which involves a complicated spatial overlap of the two modes over the cross-sectional surface S of the fiber. Note that the attenuation coefficient $\gamma \equiv \omega / 2 v_g Q$ of each mode (the inverse of their respective attenuation length) is proportional to their lifetime Q and group velocity v_g.

We focus on fibers comprising chalcogenide/polyethersulfone (PES) composites of permittivities $\epsilon_{As_2Se_3} = 5.8125$ and $\epsilon_{PES} = 2.4025$ at telecom wavelengths. Although our technique can be readily applied to design the requisite properties at any given wavenumber k and for any desired polarization, we specifically focus on designs for operation at wavenumbers in the range $0.1(2\pi/\lambda) < k_{opt} < 2.3(2\pi/\lambda)$, with λ denoting the corresponding vacuum wavelength and k_{opt} the optimized wavenumber. We consider both leaky and guided modes above and below the PES lightline $\omega = ck/\sqrt{\epsilon_{PES}}$, respectively, along with different choices or transverse electric TE_{01} and transverse magnetic TM_{01} polarizations. TE_{01} modes are those polarized along the plane of the fiber and consist primarily of circulating E_x and E_y electric fields [78], while TM_{01} modes have electric fields E_z polarized mainly along the propagation direction z.

The top insets in Fig. 2 show an inverse-designed fiber cross section that supports phased-matched TM_{01} fundamental and third-harmonic modes (with profiles superimposed on the insets) at $k_{opt} = k_1 = 1.4(2\pi/\lambda)$. To ensure that the optimization algorithm selectively finds TM_{01} modes, we employ a magnetic current $\mathbf{J}_1 \sim \nabla \times \delta(\mathbf{r})\hat{z}$ as the source in Eq. (5), resulting in electric fields of the desired polarization. The fiber cross section is represented by a $3\lambda \times 3\lambda$ computational cell consisting of 300 pixel × 300 pixel, where the size of each pixel is $0.01\lambda \times 0.01\lambda$. From Fig. 2 (inset), it is clear that both the fundamental and third-harmonic modes are well confined to the fiber core and exhibit substantial modal overlaps, while again, the phase-matching condition is automatically satisfied by the optimization process, with $k_3 = 3k_{opt}$. We find that $|\beta_3|^2 \approx 2 \times 10^4 (\chi^{(3)}/\lambda^4)$ is almost 4 orders of magnitude larger than

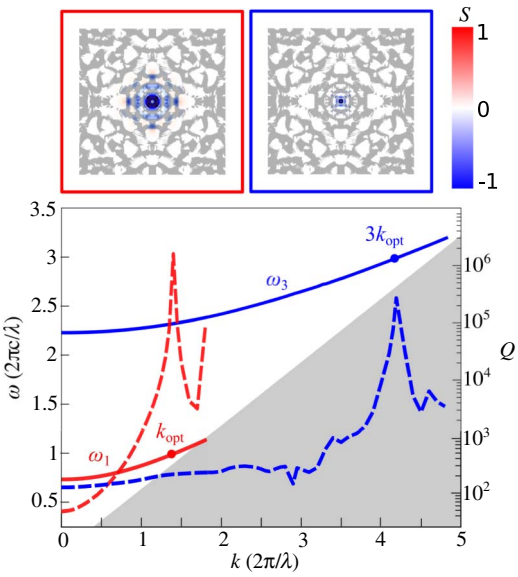

Fig. 2. Dispersion relations (solid line) and radiative lifetimes Q (dashed line) versus propagation wavenumber k of TM_{01} fundamental ω_1 (red) and third-harmonic ω_3 (blue) modes in a chalcogenide/PES fiber optimized to achieve frequency matching $\omega_3 = 3\omega_1$ and large nonlinear overlaps at $k_{opt} = 1.4(2\pi/\lambda)$. The shaded area in gray indicates regions lying below the chalcogenide light cone. The top insets show the fiber cross section overlaid with corresponding power densities at ω_1 (left) and ω_3 (right).

what has been demonstrated in standard plain fibers, which have typical values of $|\beta_3|^2 \lesssim 2(\chi^{(3)}/\lambda^4)$ [77]. Figure 2 shows the dispersion of the two leaky modes (solid lines), with the PES lightline represented by the gray region and their corresponding dimensionless lifetimes, around $Q_1 \approx 10^6$ and $Q_3 \approx 10^5$ at k_{opt}, plotted as dashed lines. Noticeably, while the fiber is optimized to ensure phase matching at a single k_{opt}, any phase mismatch remains small in the vicinity of $k \approx k_{opt}$. In fact, even for $k \ll k_{opt}$, the frequency difference is found to be only around 1%. Technically, the only factor limiting the lifetimes is the finite computational cross-section (imposed by the finite computational cell), with much larger lifetimes possible for larger cross sections. Away from k_{opt}, the quality factors decrease while remaining relatively large over a wide range of k. Considering the group velocity v_g around k_{opt}, we find that the attenuation length of the fiber $L_{rad} = 1/\gamma \approx 2 v_g Q/\omega = 1.66 \times 10^5 \lambda$. We note that while the fiber supports multiple modes around these wavelengths, the only modes near k_{opt} are those discovered by the optimization and shown in the figure.

Figure 3 shows the β_3 corresponding to fibers optimized for operation at different values of k_{opt} and polarizations, and obtained by application of either topology (squares or circles) or shape (triangles) optimization. The figure shows a general trend in which β_3 decreases with increasing k_{opt} for both polarizations, except that TM_{01} fibers tend to exhibit non-monotonic behavior, with β_3 increasing sharply at an intermediate $k_{opt} \approx 2\pi/\lambda$ below the lightline, above which it drops significantly before increasing again in the guided regime, peaking again at $k_{opt} \approx 1.7(2\pi/\lambda)$ before plummeting once again. We suspect that this complicated behavior is not a consequence of any

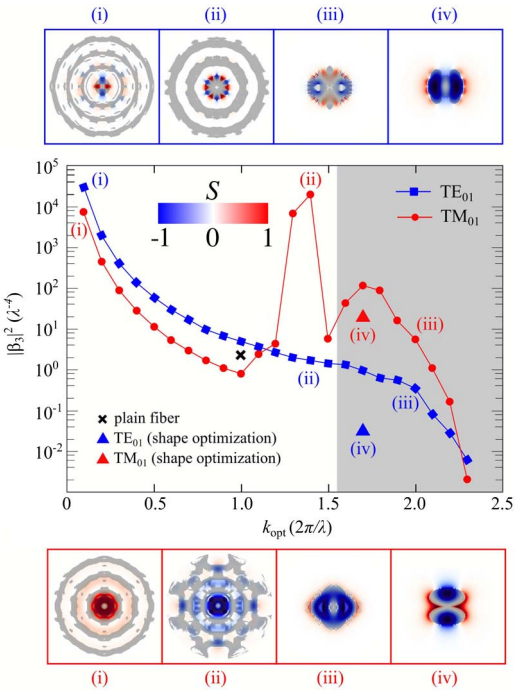

Fig. 3. Nonlinear overlap factor $|\beta_3|^2$ corresponding to fundamental and third-harmonic modes in fibers that have been optimized to ensure phase-matched modes ($k_3 = 3k_{\text{opt}}$) at various fundamental-mode propagation wavenumbers k_{opt}, for both TE_{01} (blue) and TM_{01} (red) polarizations, by the application of either topology (circles or squares) or shape (triangles) optimization. The gray-shaded area denotes the regime of guided modes below the chalcogenide lightline. For comparison, also shown is $|\beta_3|^2$ (black cross) of a standard plain fiber manually designed for operation at $\omega_1 = 0.914(2\pi c/\lambda)$ and $k_1 = 0.992(2\pi/\lambda)$ [77]. Shown as insets are fiber cross sections along with power densities of fundamental modes optimized at four different $k_{\text{opt}} = \{0.1, 1.4, 1.7, 2.0\}(2\pi/\lambda)$ for both TE_{01} (upper insets) and TM_{01} (lower insets), with (i)–(iii) obtained via topology optimization and (iv) via shape optimization.

fundamental limitation or physical consideration, but rather stems from the optimization algorithm getting stuck in local minima. Regardless, our results provide a proof-of-principle of the existence of fiber designs with performance characteristics that can greatly surpass those of traditional, hand-designed fibers. Furthermore, Fig. 3 shows typical fiber cross sections at selective k_{opt}, along with their corresponding superimposed (fundamental) mode profiles, illustrating the fabricability of the structures, in which the structure via shape optimization [Fig. 3(iv)] is easiest for fabrication.

Finally, we provide estimates of the power requirements associated with these fiber designs. We find that, for a TM_{01} fiber operating at $k_{\text{opt}} = 1.4(2\pi/\lambda)$ and at a wavelength of $\lambda = 1$ μm, conversion efficiencies of 50% can be attained at relatively small pump powers $P_1 \approx 1.7$ mW over a fiber segment $L \approx 3$ cm, while the corresponding (radiative) attenuation lengths are ≈17 cm. For comparison, plain silica fibers [77] exhibit mode-overlap factors $\beta_3 \approx 2(\chi^{(3)}/\lambda^2)$, leading to conversion efficiencies of the order of 10^{-8}% for the same input power and fiber length. (Note that typical PhC fibers rely on enhancements such as slow light effects [47], exhibiting even poorer β_3 than that of a fiber.) Hence, the optimized structures achieve considerably ($\sim 10^9$ times) higher conversion efficiencies, an improvement that is only partially due to the larger $\chi^{(3)}$ of chalcogenide compared to glass (approximately 440 times larger). In particular, defining the normalized interaction fiber length $L(\chi^{(3)})$, which removes any source of material enhancement, we find that the optimized fiber leads to a factor of 10^4 enhancement. Similarly, we find that a TE_{01} fiber operating at $k_{\text{opt}} = 0.2(2\pi/\lambda)$ results in a factor of 10^3 enhancement compared to plain fibers.

4. SECOND-HARMONIC GENERATION IN METASURFACES

Metasurfaces offer an advantageous platform for realizing complicated beam generation and wavefront shaping over extended surfaces [79] and have recently been exploited in conjunction with nonlinear materials as a means of generating and controlling light at multiple wavelengths [43,48,80,81]. A typical nonlinear metasurface can suffer from poor frequency-conversion efficiencies due to a combination of weak confinement, material absorption, and sub-optimal mode overlaps. In particular, typical designs exploit plasmonic [38–40,50] or all-dielectric [42,49] elements comprising simple shapes distributed over a unit cell, including split ring resonators [38,40,50], cross bars [39], and cylindrical posts [49], with the main focus being that of satisfying the requisite frequency- and phase-matching condition [82]. Here, we show that inverse design can not only facilitate the enforcement of frequency- and phase-matching requirements but also allow further enhancements stemming from the intentional engineering of nonlinear modal overlaps, often neglected in typical designs.

To achieve large second-harmonic generation efficiencies, a metasurface must support two extended resonances at frequencies ω_1 and $\omega_2 = 2\omega_1$ and wavevectors satisfying the phase-matching condition $\mathbf{k}_2 = 2\mathbf{k}_1$. As illustrated schematically in Fig. 4(a), a typical setup consists of an incident wave of power per unit cell P_1 at some frequency and angle (described by wavenumber $\mathbf{k}_1$) and a corresponding output harmonic wave of power per unit cell, P_2. In the small-signal regime, the output power $P_2 \propto P_1^2$ scales quadratically with P_1, resulting in a conversion efficiency per unit cell of

$$\eta = \frac{P_2}{P_1^2} = \frac{Q_1^4 Q_2^2}{Q_{1,\text{rad}}^2 Q_{2,\text{rad}}} \frac{|\beta_2|^2 \lambda_1}{\pi \epsilon_0 c}, \tag{7}$$

where Q and Q_{rad} denote total and radiative dimensionless lifetimes and β_2 the nonlinear overlap factor:

$$\beta_2 = \frac{\int \mathrm{d}V \chi^{(2)} \mathbf{E}_2^* \cdot \mathbf{E}_1^2}{\left(\int \mathrm{d}V \epsilon_1 |\mathbf{E}_1|^2\right)\left(\sqrt{\int \mathrm{d}V \epsilon_2 |\mathbf{E}_2|^2}\right)}. \tag{8}$$

Note that here the conversion efficiency is defined as the efficiency per unit cell for such an extended surface, hence the volume integration is performed inside a unit cell.

We now apply our optimization framework to discover new all-dielectric three-dimensional metasurfaces, with the permittivity of the medium ϵ_{GaP} taken to be that of gallium phosphide near telecom wavelengths [83,84]. Note, however, that the same framework can be easily extended to design plasmonic

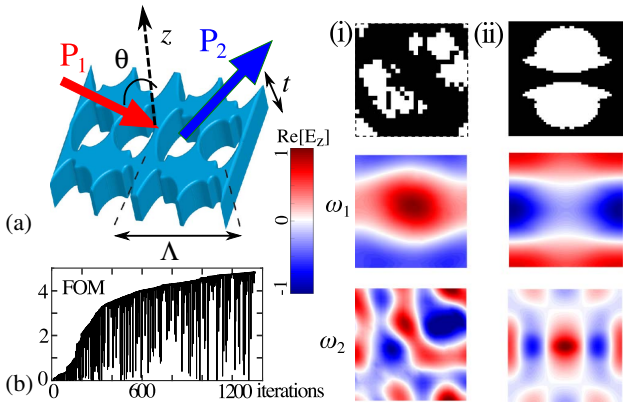

Fig. 4. (a) Schematic illustration of second-harmonic generation in a square-lattice metasurface of finite thickness t and period $\Lambda \times \Lambda$. Shown to the right are dielectric profiles and mode profiles $|\mathbf{E}|^2$ corresponding to two inverse-designed metasurfaces, both over single unit cells and $z = 0$ cross sections. The structures are optimized to ensure frequency and phase matching for light incident at (i) an angle $\theta = 3°$ or (ii) normal incidence. Dark (white) represents gallium phosphide (vacuum) regions. (b) Convergence of the objective function with respect to iteration number, leading to structure (ii).

surfaces. The metasurfaces illustrated schematically in Fig. 4 are square PhC slabs of in-plane periodicity $\Lambda \times \Lambda$ and finite thickness t. To ensure fabricability, here we consider z-invariant structures, in which the optimization parameters are taken to lie in the plane perpendicular to the z axis, resulting in a structure that can be fabricated by etching. As a proof-of-principle, we consider metasurfaces suspended in air, while the same framework can be easily applied to include any substrate [27].

Figure 4 shows cross sections of the unit cell of two GaP metasurfaces of thickness $t = 612$ nm and $\Lambda = 480$ nm, designed for operation at a fundamental frequency $\omega_1 = 1.57 \times 10^{15}$ rad/s ($\lambda = 1.2$ μm) so as to satisfy both frequency- and phase-matching conditions. Also shown are the corresponding fundamental and harmonic mode profiles. The structure on the left is optimized for operation at an incident angle $\theta \approx 3.6°$ relative to the out-of-plane axis, and is found to exhibit large radiative lifetimes $Q^{\text{rad}}_{1(2)} \approx 6(2) \times 10^4$ and overlap factor $|\beta_2|^2 = 1.6 \times 10^{-3}(\chi^{(2)}/\lambda^3)$. The structure on the right is instead optimized for operation at normal incidence, resulting in a slightly smaller $|\beta_2|^2 = 4 \times 10^{-4}(\chi^{(2)}/\lambda^3)$. Because of the symmetry of the structure, the modes exhibit infinite lifetimes (and, hence, are technically dark modes), though in practice, fabrication imperfections necessarily lead to finite lifetimes. Furthermore, Fig. 4(b) illustrates the convergence of the TO optimization process to achieve structure (i), converged within $\sim 10^3$ iterations. Table 1 compares a few of the relevant FOMs for representative metasurface designs, which include both plasmonic and dielectric structures. Although comparing β_2 appears to be impossible due to a surprising lack of relevant modal parameters in these studies [38,39,49,50], such as the absence of radiative and dissipative quality factors, we find that the optimized designs exhibit orders of magnitude larger conversion efficiencies. While it is difficult to distinguish the relative impact of the mode lifetimes and overlap factors, arguably, the optimized structures overcome several limitations associated with previous designs. On the one hand, plasmonic structures exhibit tightly confined modes and therefore lead to large nonlinear overlaps, but absorptive losses and weak material nonlinearities imply that they suffer from small lifetimes. On the other hand, several of the proposed all-dielectric metasurfaces have had negligible material losses and, hence, larger lifetimes, but have not been designed to ensure large nonlinear overlaps.

Table 1. Representative Second-Harmonic Generation FOMs for Both Hand- and Inverse-Designed Metasurfaces, Including $\chi^{(2)}$, Fundamental Wavelength λ_1, and Conversion Efficiency η per Unit Cell[a]

Structure	$\chi^{(2)}$ (nm/V)	λ_1 (μm)	$\eta/(\chi^{(2)})^2$
Gold split resonators [38]	250	10	2.1×10^{11}
Gold split resonators [50]	1.3	3.4	3.8×10^{11}
Gold cross bars [39]	54	8	1.4×10^{13}
All-dielectric cylinders [49]	0.2	1.02	1.6×10^{17}
Optimized design [Fig. 4]	0.1	1.2	9.6×10^{24}

[a]Most of the literature states only the net conversion efficiency for metasurfaces with finite N unit cells, which we convert to the efficiency η per unit cell.

5. CONCLUDING REMARKS

We have demonstrated an optimization approach for the design of nonlinear photonic fibers and metasurfaces. The optimized structures demonstrate very high leaky-mode lifetimes for both fundamental and harmonic modes and orders-of-magnitude larger overlap factors than traditional designs. Inverse design not only overcomes efficiency limitations of traditional index fibers and PhC metasurfaces but also greatly reduces challenges and difficulties inherent to the design process. Although in this paper we have not considered effects resulting from self- or cross-phase modulation, we expect no significant impact on the conversion efficiency in the small-signal limit, since the finite bandwidth around the designated phase-matched propagation wavevectors can potentially compensate for any small phase mismatch that might arise. At larger powers where these effects cannot be ignored, one could account and compensate for them through minor modifications to the optimization objective function, the subject of future work. Furthermore, we will consider extending our inverse-design framework to terahertz frequency generation and other nonlinear processes.

Funding. National Science Foundation (NSF) (DMR-1420541, DMR-1454836, EFMA-1640986).

REFERENCES

1. K. W. DeLong, R. Trebino, J. Hunter, and W. E. White, "Frequency-resolved optical gating with the use of second-harmonic generation," J. Opt. Soc. Am. B **11**, 2206–2215 (1994).
2. M. A. Arbore, A. Galvanauskas, D. Harter, M. H. Chou, and M. M. Fejer, "Engineerable compression of ultrashort pulses by use of second-harmonic generation in chirped-period-poled lithium niobate," Opt. Lett. **22**, 1341–1343 (1997).

3. T. F. Heinz, C. K. Chen, D. Ricard, and Y. R. Shen, "Spectroscopy of molecular monolayers by resonant second-harmonic generation," Phys. Rev. Lett. **48**, 478–481 (1982).
4. P. S. Kuo, K. L. Vodopyanov, M. M. Fejer, D. M. Simanovskii, X. Yu, J. S. Harris, D. Bliss, and D. Weyburne, "Optical parametric generation of a mid-infrared continuum in orientation-patterned GaAs," Opt. Lett. **31**, 71–73 (2006).
5. K. L. Vodopyanov, M. M. Fejer, X. Yu, J. S. Harris, Y.-S. Lee, W. C. Hurlbut, V. G. Kozlov, D. Bliss, and C. Lynch, "Terahertz-wave generation in quasi-phase-matched GaAs," Appl. Phys. Lett. **89**, 141119 (2006).
6. R. Krischek, W. Wieczorek, A. Ozawa, N. Kiesel, P. Michelberger, T. Udem, and H. Weinfurter, "Ultraviolet enhancement cavity for ultrafast nonlinear optics and high-rate multiphoton entanglement experiments," Nat. Photonics **4**, 170–173 (2010).
7. A. Vaziri, G. Weihs, and A. Zeilinger, "Experimental two-photon, three-dimensional entanglement for quantum communication," Phys. Rev. Lett. **89**, 240401 (2002).
8. S. Tanzilli, W. Tittel, M. Halder, O. Alibart, P. Baldi, N. Gisin, and H. Zbinden, "A photonic quantum information interface," Nature **437**, 116–120 (2005).
9. S. Zaske, A. Lenhard, C. A. Keßler, J. Kettler, C. Hepp, C. Arend, R. Albrecht, W.-M. Schulz, M. Jetter, P. Michler, and C. Becher, "Visible-to-telecom quantum frequency conversion of light from a single quantum emitter," Phys. Rev. Lett. **109**, 147404 (2012).
10. J. U. Fürst, D. V. Strekalov, D. Elser, M. Lassen, U. L. Andersen, C. Marquardt, and G. Leuchs, "Naturally phase-matched second-harmonic generation in a whispering-gallery-mode resonator," Phys. Rev. Lett. **104**, 153901 (2010).
11. M. M. Fejer, "Nonlinear optical frequency conversion," Phys. Today **47**, 25–32 (1994).
12. M. Soljačić and J. D. Joannopoulos, "Enhancement of nonlinear effects using photonic crystals," Nat. Mater. **3**, 211–219 (2004).
13. Y. Dumeige and P. Feron, "Wispering-gallery-mode analysis of phase-matched doubly resonant second-harmonic generation," Phys. Rev. A **74**, 063804 (2006).
14. L.-A. Wu, M. Xiao, and H. J. Kimble, "Squeezed states of light from an optical parametric oscillator," J. Opt. Soc. Am. B **4**, 1465–1476 (1987).
15. C. Simonneau, J. P. Debray, J. C. Harmand, P. Vidaković, D. J. Lovering, and J. A. Levenson, "Second-harmonic generation in a doubly resonant semiconductor microcavity," Opt. Lett. **22**, 1775–1777 (1997).
16. R. Paschotta, K. Fiedler, P. Kurz, and J. Mlynek, "Nonlinear mode coupling in doubly resonant frequency doublers," Appl. Phys. Lett. **58**, 117–122 (1994).
17. K. Koch and G. T. Moore, "Singly resonant cavity-enhanced frequency tripling," J. Opt. Soc. Am. B **16**, 448–459 (1999).
18. M. Liscidini and L. A. Andreani, "Highly efficient second-harmonic generation in doubly resonant planar microcavities," Appl. Phys. Lett. **85**, 1883–1885 (2004).
19. K. Rivoire, S. Buckley, and J. Vuckovic, "Multiply resonant high quality photonic crystal nanocavities," Appl. Phys. Lett. **99**, 013114 (2011).
20. D. Ramirez, A. W. Rodriguez, H. Hashemi, J. D. Joannopoulos, M. Solijacic, and S. G. Johnson, "Degenerate four-wave mixing in triply-resonant nonlinear Kerr cavities," Phys. Rev. A **83**, 033834 (2011).
21. Z. Lin, T. Alcorn, M. Loncar, S. Johnson, and A. Rodriguez, "High-efficiency degenerate four wave-mixing in triply," Phys. Rev. A **89**, 053839 (2014).
22. W. H. P. Pernice, C. Xiong, C. Schuck, and H. X. Tang, "Second harmonic generation in phase matched aluminum nitride waveguides and micro-ring resonators," Appl. Phys. Lett. **100**, 223501 (2012).
23. Z.-F. Bi, A. W. Rodriguez, H. Hashemi, D. Duchesne, M. Loncar, K.-M. Wang, and S. G. Johnson, "High-efficiency second-harmonic generation in doubly-resonant $\chi^{(2)}$ microring resonators," Opt. Express **20**, 7526–7543 (2012).
24. K. Rivoire, Z. Lin, F. Hatami, W. T. Masselink, and J. Vučković, "Second harmonic generation in gallium phosphide photonic crystal nanocavities with ultralow continuous wave pump power," Opt. Express **17**, 22609–22615 (2009).
25. S. Buckley, M. Radulaski, J. L. Zhang, J. Petykiewicz, K. Biermann, and J. Vučković, "Multimode nanobeam cavities for nonlinear optics: high quality resonances separated by an octave," Opt. Express **22**, 26498–26509 (2014).
26. A. Rodriguez, M. Soljačić, J. D. Joannopulos, and S. G. Johnson, "$\chi^{(2)}$ and $\chi^{(3)}$ harmonic generation at a critical power in inhomogeneous doubly resonant cavities," Opt. Express **15**, 7303–7318 (2007).
27. Z. Lin, X. Liang, M. Lončar, S. G. Johnson, and A. W. Rodriguez, "Cavity-enhanced second-harmonic generation via nonlinear-overlap optimization," Optica **3**, 233–238 (2016).
28. Z. Lin, M. Lončar, and A. W. Rodriguez, "Topology optimization of multi-track ring resonators and 2D microcavities for nonlinear frequency conversion," arXiv:1701.05628 (2017).
29. L. Goldberg and D. A. V. Kliner, "Tunable UV generation at 286 nm by frequency tripling of a high-power mode-locked semiconductor laser," Opt. Lett. **20**, 1640–1642 (1995).
30. Y. Yelin and D. Silberberg, "Laser scanning third-harmonic-generation microscopy in biology," Opt. Express **5**, 169–175 (1999).
31. P. Pantazis, J. Maloney, D. Wu, and S. E. Fraser, "Second harmonic generating (SHG) nanoprobes for in vivo imaging," Proc. Natl. Acad. Sci. USA **107**, 14535–14540 (2010).
32. D. R. Hamel, A. Fedrizzi, S. Ramelow, K. J. Resch, and T. Jennewein, "Direct generation of photon triplets using cascaded photon-pair sources," Nature **466**, 601–603 (2010).
33. K. Rivoire, S. Buckley, F. Hatami, and J. Vuckovic, "Sum-frequency generation in doubly resonant GaP photonic crystal nanocavities," Appl. Phys. Lett. **98**, 263113 (2011).
34. S. Buckley, M. Radulaski, K. Biermann, and J. Vuckovic, "Second harmonic generation in photonic crystal cavities in (111)-oriented GaAs," arXiv:1308.6051v1 (2013).
35. D. W. Hall, M. A. Newhouse, N. F. Borrelli, W. H. Dumbaugh, and D. L. Weidman, "Nonlinear optical susceptibilities of high-index glasses," Appl. Phys. Lett. **54**, 1293–1295 (1989).
36. R. Ahmad, M. Soljacic, M. Ibanescu, T. Engeness, M. Skorobogatly, S. Johnson, O. Weisberg, Y. Fink, L. Pressman, W. King, E. Anderson, and J. D. Joannopoulos, "High index-contrast fiber waveguides and applications," U.S. patent 6,788,864 B2 (April 12, 2004).
37. M. Lapine, I. V. Shadrivov, and Y. S. Kivshar, "Colloquium: nonlinear metamaterials," Rev. Mod. Phys. **86**, 1093–1123 (2014).
38. S. Campione, A. Benz, M. B. Sinclair, F. Capolino, and I. Brener, "Second harmonic generation from metamaterials strongly coupled to intersubband transitions in quantum wells," Appl. Phys. Lett. **104**, 131104 (2014).
39. J. Lee, M. Tymchenko, C. Argyropoulos, P.-Y. Chen, F. Lu, F. Demmerle, G. Boehm, M.-C. Amann, A. Alu, and M. A. Belkin, "Giant nonlinear response from plasmonic metasurfaces coupled to intersubband transitions," Nature **511**, 65–69 (2014).
40. O. Wolf, S. Campione, A. Benz, A. P. Ravikumar, S. Liu, T. S. Luk, E. A. Kadlec, E. A. Shaner, J. F. Klem, M. B. Sinclair, and I. Brener, "Phased-array sources based on nonlinear metamaterial nanocavities," Nat. Commun. **6**, 7667 (2015).
41. K. O'Brien, H. Suchowski, J. Rho, A. Salandrino, B. Kante, X. Yin, and X. Zhang, "Predicting nonlinear properties of metamaterials from the linear response," Nat. Mater. **14**, 379–383 (2015).
42. Y. Yang, W. Wang, A. Boulesbaa, I. I. Kravchenko, D. P. Briggs, A. Puretzky, D. Geohegan, and J. Valentine, "Nonlinear Fano-resonant dielectric metasurfaces," Nano Lett. **15**, 7388–7393 (2015).
43. N. Segal, S. Keren-Zur, N. Hendler, and T. Ellenbogen, "Controlling light with metamaterial-based nonlinear photonic crystals," Nat. Photonics **9**, 180–184 (2015).
44. J. Butet, P.-F. Brevet, and O. J. Martin, "Optical second harmonic generation in plasmonic nanostructures: from fundamental principles to advanced applications," ACS Nano **9**, 10545–10562 (2015).
45. A. Bétourné, Y. Quiquempois, G. Bouwmans, and M. Douay, "Design of a photonic crystal fiber for phase-matched frequency doubling or tripling," Opt. Express **16**, 14255–14262 (2008).
46. F. G. Omenetto, A. J. Taylor, M. D. Moores, J. Arriaga, J. C. Knight, W. J. Wadsworth, and P. St. J. Russell, "Simultaneous generation of spectrally distinct third harmonics in a photonic crystal fiber," Opt. Lett. **26**, 1158–1160 (2001).
47. B. Corcoran, C. Monat, C. Grillet, D. J. Moss, B. J. Eggleton, T. P. White, L. O'Faolain, and T. F. Krauss, "Green light emission in silicon

through slow-light enhanced third-harmonic generation in photonic-crystal waveguides," Nat. Photonics **3**, 206–210 (2009).
48. G. Li, S. Zhang, and T. Zentgraf, "Nonlinear photonic metasurfaces," Nat. Rev. Mater. **2**, 17010 (2017).
49. S. Liu, M. B. Sinclair, S. Saravi, G. A. Keeler, Y. Yang, J. Reno, G. M. Peake, F. Setzpfandt, I. Staude, T. Pertsch, and I. Brener, "Resonantly enhanced second-harmonic generation using III–V semiconductor all-dielectric metasurfaces," Nano Lett. **16**, 5426–5432 (2016).
50. O. Wolf, A. A. Allerman, X. Ma, J. R. Wendt, A. Y. Song, E. A. Shaner, and I. Brener, "Enhanced optical nonlinearities in the near-infrared using III-nitride heterostructures coupled to metamaterials," Appl. Phys. Lett. **107**, 151108 (2015).
51. M. Tymchenko, J. S. Gomez-Diaz, J. Lee, N. Nookala, M. A. Belkin, and A. Alù, "Gradient nonlinear pancharatnam-berry metasurfaces," Phys. Rev. Lett. **115**, 207403 (2015).
52. J. D. Joannopoulos, S. G. Johnson, J. N. Winn, and R. D. Meade, *Photonic Crystals: Molding the Flow of Light*, 2nd ed. (Princeton University, 2008).
53. S. Molesky, Z. Lin, A. Piggot, W. Jin, J. Vuckovic, and A. W. Rodriguez, "Outlook for inverse design in nanophotonics," arXiv:1801.06715 (2018).
54. W. J. Kim and J. D. O'Brien, "Optimization of a two-dimensional photonic-crystal waveguide branch by simulated annealing and the finite-element method," J. Opt. Soc. Am. B **21**, 289–295 (2004).
55. B. S. Darki and N. Granpayeh, "Improving the performance of a photonic crystal ring-resonator-based channel drop filter using particle swarm optimization method," Opt. Commun. **283**, 4099–4103 (2010).
56. M. Minkov and V. Savona, "Automated optimization of photonic crystal slab cavities," Sci. Rep. **4**, 5124 (2014).
57. A. Gondarenko, S. Preble, J. Robinson, L. Chen, H. Lipson, and M. Lipson, "Spontaneous emergence of periodic patterns in a biologically inspired simulation of photonic structures," Phys. Rev. Lett. **96**, 143904 (2006).
58. J. Jensen and O. Sigmund, "Topology optimization for nano-photonics," Laser Photon. Rev. **5**, 308–321 (2011).
59. N. Aage, E. Andreassen, B. S. Lazarov, and O. Sigmund, "Giga-voxel computational morphogenesis for structural design," Nature **550**, 84–86 (2017).
60. X. Liang and S. G. Johnson, "Formulation for scalable optimization of microcavities via the frequency-averaged local density of states," Opt. Express **21**, 30812–30841 (2013).
61. D. Liu, L. H. Gabrielli, M. Lipson, and S. G. Johnson, "Transformation inverse design," Opt. Express **21**, 14223–14243 (2013).
62. A. Y. Piggott, J. Lu, T. M. Babinec, K. G. Lagoudakis, J. Petykiewicz, and J. Vuckovic, "Inverse design and implementation of a wavelength demultiplexing grating coupler," Sci. Rep. **4**, 7210 (2014).
63. H. Men, K. Y. K. Lee, R. M. Freund, J. Peraire, and S. G. Johnson, "Robust topology optimization of three-dimensional photonic-crystal band-gap structures," arXiv:1405.4350 (2014).
64. A. Y. Piggott, J. Lu, K. G. Lagoudakis, J. Petykiewicz, T. M. Babinec, and J. Vuckovic, "Inverse design and demonstration of a compact and broadband on-chip wavelength demultiplexer," Nat. Photonics **9**, 374–377 (2015).
65. B. Shen, P. Wang, and R. Menon, "An integrated-nanophotonics polarization beamsplitter with $2.4 \times 2.4\ \mu m^2$ footprint," Nat. Photonics **9**, 378–382 (2015).
66. G. Strang, *Computational Science and Engineering* (Wellesley-Cambridge, 2007), Vol. **791**.
67. J. D. Deaton and R. V. Grandhi, "A survey of structural and multidisciplinary continuum topology optimization: post 2000," Struct. Multidiscip. Optim. **49**, 1–38 (2014).
68. M. P. Bendsøe, O. Sigmund, M. P. Bendsøe, and O. Sigmund, *Topology Optimization by Distribution of Isotropic Material* (Springer, 2004).
69. M. Y. Wang, X. Wang, and D. Guo, "A level set method for structural topology optimization," Comput. Methods Appl. Mech. Eng. **192**, 227–246 (2003).
70. J. Haslinger and R. A. Mäkinen, *Introduction to Shape Optimization: Theory, Approximation, and Computation* (SIAM, 2003).
71. K. Svanberg, "A class of globally convergent optimization methods based on conservative convex separable approximations," SIAM J. Optim. **12**, 555–573 (2002).
72. F. Wang and O. Sigmund, "Optimization of photonic crystal cavities," in *International Conference on Numerical Simulation of Optoelectronic Devices (NUSOD)* (IEEE, 2017), pp. 39–40.
73. R. W. Boyd, *Nonlinear Optics* (Academic, 1992).
74. A. Taflove and S. C. Hagness, *Computational Electrodynamics: The Finite-Difference Time-Domain Method* (Artech, 2000).
75. B. Temelkuran, S. D. Hart, G. Benoit, J. D. Joannopoulos, and Y. Fink, "Wavelength-scalable hollow optical fibres with large photonic bandgaps for CO_2 laser transmission," Nature **420**, 650–653 (2002).
76. X. Feng, T. Monro, P. Petropoulos, V. Finazzi, and D. Hewak, "Solid microstructured optical fiber," Opt. Express **11**, 2225–2230 (2003).
77. V. Grubsky and A. Savchenko, "Glass micro-fibers for efficient third harmonic generation," Opt. Express **13**, 6798–6806 (2005).
78. G. P. Agrawal, *Fiber-Optic Communication Systems* (Wiley, 2012), Vol. **222**.
79. N. Yu and F. Capasso, "Flat optics with designer metasurfaces," Nat. Mater. **13**, 139–150 (2014).
80. L. Michaeli, S. Keren-Zur, O. Avayu, H. Suchowski, and T. Ellenbogen, "Nonlinear surface lattice resonance in plasmonic nanoparticle arrays," Phys. Rev. Lett. **118**, 243904 (2017).
81. S. Keren-Zur, O. Avayu, L. Michaeli, and T. Ellenbogen, "Nonlinear beam shaping with plasmonic metasurfaces," ACS Photon. **3**, 117–123 (2015).
82. A. Krasnok, M. Tymchenko, and A. Alù, "Nonlinear metasurfaces: a paradigm shift in nonlinear optics," arXiv:1706.07563 (2017).
83. W. Bond, "Measurement of the refractive indices of several crystals," J. Appl. Phys. **36**, 1674–1677 (1965).
84. I. Shoji, T. Kondo, A. Kitamoto, M. Shirane, and R. Ito, "Absolute scale of second-order nonlinear-optical coefficients," J. Opt. Soc. Am. B **14**, 2268–2294 (1997).